AIAA JOURNAL
Vol. 45, No. 6, June 2007

Computational Study of Magnetogasdynamic Inlet Flow Control on a Flight-Scale Scramjet

Martin F. Lindsey* and Richard J. McMullan†
U.S. Air Force Institute of Technology, Wright–Patterson Air Force Base, Ohio 45433
and
Datta V. Gaitonde‡ and José A. Camberos§
U.S. Air Force Research Laboratory, Wright–Patterson Air Force Base, Ohio 45433

DOI: 10.2514/1.24185

Results of computational work demonstrating magnetogasdynamic flow control within the internal inlet of a full-scale, Mach 10 scramjet engine simulation are presented. As part of the analysis, a control volume approach with an electron beam ionization model is presented for the first time in the context of the established computational method used. We conclude that applying magnetogasdynamic interaction entirely upstream of a expansion-induced flow separation zone was not effective at improving the inlet efficiency. For most parameters tested, any pressure gains incurred in the region of electromagnetic interaction were all but negated by an additional sidewall expansion at the inlet throat. Magnetogasdynamic acceleration can efficiently reduce the net inlet drag in some cases while minimizing the increase in heat transfer and decrease in overall efficiency measures. Finally, placement of the electromagnetic interaction region near the wall was the most important factor in determining the wall heat transfer and proved to be a relatively efficient method for limiting drag increases. However, further work is recommended to determine the optimum distance from the wall to target the electron beam ionization.

Nomenclature

A	=	area
B	=	magnetic flux density
c_v, c_p	=	specific heats
E	=	electric field
e_t	=	mass-specific total energy
F	=	control volume force
h	=	mass-specific static enthalpy
h_t	=	mass-specific total enthalpy
J	=	Jacobian of transformation
j	=	conduction current
L	=	length
$\dot{m}$	=	mass flow rate
p	=	pressure
P_{gen}	=	generated power
P_{ion}	=	ionization power
Q	=	interaction parameter
$\dot{Q}_{\text{ht}}$	=	control volume heat transfer
q	=	heat conduction
t	=	time
u, v, w	=	velocity components
V	=	velocity
$\dot{W}_{\text{EM}}$	=	control volume EM energy interaction
x, y, z	=	spatial coordinates
γ	=	ratio of specific heats
$\Delta s/C_p$	=	dimensionless entropy rise
δ	=	Kronecker delta function
η_c	=	adiabatic compression efficiency
η_g	=	enthalpy extraction ratio
η_{KE}	=	kinetic energy efficiency
μ	=	molecular viscosity
ξ, η, ζ	=	generalized coordinates
π_c	=	total pressure ratio
ρ	=	density
σ	=	electrical conductivity
τ	=	viscous stress tensor or generalized time

Subscripts

e, i, o, x	=	control volume indices
i, j, k	=	indices
0	=	reference condition

Presented as Paper 371 at the 44th AIAA Aerospace Sciences Meeting and Exhibit, Reno, NV, 9–12 January 2006; received 24 March 2006; revision received 4 August 2006; accepted for publication 14 November 2006.

*Major, U.S. Air Force, Ph.D.; currently U.S. Air Force Research Laboratory, Propulsion Directorate, Aerospace Propulsion Division, Propulsion Sciences Branch, Wright–Patterson Air Force Base, OH 45433. Member AIAA.

†Major, U.S. Air Force, Assistant Professor. Senior Member AIAA.

‡Technology Area Leader, Air Vehicles Directorate. Associate Fellow AIAA.

§Research Aerospace Engineer, Air Vehicles Directorate. Associate Fellow AIAA.

I. Introduction

IN RECENT years, numerous techniques for using electromagnetic (EM) fields to locally improve scramjet flow have been proposed [1–4]. Additionally, a few more ambitious proposals have proposed using these same concepts to provide both electrical energy to power the flow ionizer and augment the vehicle's thrust. Because scramjet vehicles are geometrically optimized for a single design point, it is assumed that a significant portion of their mission will be spent operating at off-design conditions. In addition, even while operating at design conditions, there will be regions of locally ill-conditioned flow due to geometric or other constraints. Therefore, localized flow control aims to mitigate these ill-conditioned regions or enhance favorable flow qualities. These flow control techniques may be the deciding factor in the success or failure of a particular engine design.

Manipulating the boundary layer is an example of local flow control that preliminary studies have demonstrated may benefit from magnetogasdynamic (MGD) interaction. This is especially true with respect to controlling the transition from laminar to turbulent flow as well as increasing the near-wall flow momentum to prevent separation and potential inlet unstart. The shock structure within 3-D

inlet flows is incredibly complex as several researchers [5–8] have shown, where common detrimental features include sidewall interaction, low momentum vortical structures, and large areas of flow separation. These structures are detrimental to the flow because they increase total pressure losses, prevent a smooth flowfield at the combustor entrance, and in the worst instances may cause inlet unstart.

The remainder of this article addresses how MGD was applied to a computational model of a Mach 10 scramjet inlet to improve both compression and efficiency. In the next section, we begin with a presentation of the governing equations of MGD in the supersonic, weakly ionized plasma environment. This includes a description of the numerical methods employed. As part of the analysis, a control volume approach with an electron beam ionization model is presented for the first time as a technique for postprocessing the established computational method. Combining the computational fluid dynamics (CFD) and postprocessing methods allows for a relatively straightforward engine cycle performance analysis, including electromagnetic interaction. These building blocks are combined and demonstrated in Sec. III as the results for a flight-scale scramjet inlet parameter study are presented. This study attempted to mitigate observed detrimental inlet flow structures and thus improve the inlet efficiency. This is done by exploring different combinations of conductivity profile, relative strength of the electromagnetic interaction, and load factor. Finally, Sec. IV summarizes the conclusions reached.

II. Governing Equations, Numerical Methods, and Performance Measures

A. Magnetogasdynamic Equations

The assumptions and derivation of the governing equations of MGD flow are well established [9–12]. Their implementation in the U.S. Air Force Research Laboratory (AFRL) research code used here has likewise been well documented by the authors [6,13–16]. In summary, the aerospace environment of interest for this type of problem is characterized as weakly ionized. A weakly ionized flow has a relatively low magnetic Reynolds number. Under these conditions, a relatively large magnetic field is needed to obtain a reasonable fluid–magnetic interaction parameter of order one, $Q = \sigma_0 B_0^2 L_0/(\rho_0 V_0)$. These assumptions lead to a simplified combination of the Maxwell equations for electromagnetics and the Navier–Stokes equations for fluid flow, in which the interaction between electromagnetic fields and electrically conducting gases in a continuum reduces to source terms for the Lorentz vector force ($\boldsymbol{j} \times \boldsymbol{B}$) and energy interaction term ($\boldsymbol{E} \cdot \boldsymbol{j}$) in the Navier–Stokes momentum and energy equations, respectively. The nondimensional governing equations for the overall mass conservation, momentum conservation, and energy conservation are therefore given by Eqs. (1–3), respectively:

$$\frac{\partial \rho}{\partial t} + \frac{\partial(\rho V_i)}{\partial x_i} = 0 \tag{1}$$

$$\frac{\partial(\rho V_i)}{\partial t} + \frac{\partial(\rho V_i V_j)}{\partial x_j} + \frac{\partial(p\delta_{ij})}{\partial x_j} - \frac{1}{Re}\frac{\partial \tau_{ij}}{\partial x_j} = Q(\boldsymbol{j} \times \boldsymbol{B}) \tag{2}$$

$$\frac{\partial(\rho e_t)}{\partial t} + \frac{\partial(\rho V_i h_t)}{\partial x_i} - \frac{1}{Re}\frac{\partial(\tau_{ij} V_j)}{\partial x_i} - \frac{1}{(\gamma-1)PrM^2Re}\frac{\partial q_i}{\partial x_i} = Q(\boldsymbol{E} \cdot \boldsymbol{j}) \tag{3}$$

In these equations, V_i, $V_j = \{u, v, w\}$ is the velocity vector, $\boldsymbol{B}$ and $\boldsymbol{E}$ are the magnetic flux and electric field, respectively, q_j is the heat conduction term, τ_{ij} is the shear stress tensor, $h_t = h + \frac{1}{2} V_i V_i$ is the total enthalpy, and $e_t = h_t - \frac{p}{\rho}$ is the total energy. The nondimensional parameters are the Reynolds number $Re = \rho_0 V_0 L_0/\mu_0$, the interaction parameter Q, the Prandtl number Pr, and the Mach number M. The transport properties of molecular viscosity μ is obtained using Sutherland's law.

The induced magnetic field is negligible for these low magnetic Reynolds number flows. The magnetic flux $\boldsymbol{B}$ is the imposed field. Therefore, electrical current $\boldsymbol{j}$ in the source terms for the Lorentz force and energy interaction is obtained from the phenomenological form of the generalized nondimensional Ohm's law as follows [17]:

$$\boldsymbol{j} = \sigma(\boldsymbol{E} + \boldsymbol{V} \times \boldsymbol{B}) \tag{4}$$

where σ is the electrical conductivity tensor calculated as products of modified Gaussians [6].

Equations (1–3) can be written in flux vector form as

$$\frac{\partial \boldsymbol{U}}{\partial t} + \frac{\partial \boldsymbol{E}}{\partial x} + \frac{\partial \boldsymbol{F}}{\partial y} + \frac{\partial \boldsymbol{G}}{\partial z} = \mathbf{S} \tag{5}$$

where $\boldsymbol{U} = \{\rho, \rho u, \rho v, \rho w, \rho e_t\}$ is the solution vector and $\boldsymbol{E}$, $\boldsymbol{F}$, and $\boldsymbol{G}$ contain the inviscid and viscous fluxes in each direction. The source term $\mathbf{S}$ is

$$\mathbf{S} = \begin{bmatrix} 0 \\ Q(j_y B_z - j_z B_y) \\ Q(j_z B_x - j_x B_z) \\ Q(j_x B_y - j_y B_x) \\ Q(E_x j_x + E_y j_y + E_z j_z) \end{bmatrix} \tag{6}$$

The various vectors of Eq. (5) have been detailed in [15,18].

To treat physically complex domains, the governing equations are mapped to curvilinear coordinates through a transformation with the following generalized coordinates: $\tau = \tau(t)$, $\xi = \xi(x, y, z)$, $\eta = \eta(x, y, z)$, $\zeta = \zeta(x, y, z)$. The strong conservation form is employed to obtain

$$\frac{\partial \hat{\boldsymbol{U}}}{\partial \tau} + \frac{\partial \hat{\boldsymbol{E}}}{\partial \xi} + \frac{\partial \hat{\boldsymbol{F}}}{\partial \eta} + \frac{\partial \hat{\boldsymbol{G}}}{\partial \zeta} = \hat{\mathbf{S}} \tag{7}$$

with J representing the Jacobian of the transformation, $\hat{\boldsymbol{U}} = \boldsymbol{U}/J$, $\hat{\mathbf{S}} = \mathbf{S}/J$ and the contravariant fluxes

$$\hat{\boldsymbol{E}} = \frac{1}{J}(\boldsymbol{E}\xi_x + \boldsymbol{F}\xi_y + \boldsymbol{G}\xi_z) \qquad \hat{\boldsymbol{F}} = \frac{1}{J}(\boldsymbol{E}\eta_x + \boldsymbol{F}\eta_y + \boldsymbol{G}\eta_z)$$
$$\hat{\boldsymbol{G}} = \frac{1}{J}(\boldsymbol{E}\zeta_x + \boldsymbol{F}\zeta_y + \boldsymbol{G}\zeta_z) \tag{8}$$

To simulate fine-scale turbulence, the code uses the popular two-equation k–ϵ model, where k is the turbulence kinetic energy and ϵ is the dissipation. New terms added to the model mimic some of the anticipated effects of the magnetic field in a simple yet effective manner. The mean flow equations were modified by replacing the molecular viscosity μ with the sum, $\mu + \mu_t$, where μ_t is the turbulent eddy viscosity and introducing the turbulent Prandtl number ($Pr_t = 0.9$) in the standard fashion [15,18].

B. Numerical Methods

Because the influence of the magnetic and electric fields contributions are restricted to the source terms of the governing equations, conventional CFD techniques are incorporated to discretize the inviscid and viscous fluxes [15,18]. The solver includes both the Roe flux difference and van Leer flux splitting schemes for determining the inviscid fluxes in each generalized coordinate direction. Solution monotonicity is assured with the use of a harmonic limiter. When higher accuracy is needed, a series of compact-difference methods can be incorporated. The viscous fluxes in each generalized coordinate direction can be discretized using either central differences or compact differences. For this study, the Roe flux difference scheme was used along with MUSCL variable extrapolation and the van Leer harmonic limiter to provide nominal third-order spatial accuracy [14,15].

The code includes the option of either an explicit Runge–Kutta time integration method or an implicit Beam–Warming time integration method [15,18]. Explicit schemes severely limit the time step size based on the size of the cells in the physical domain. To avoid this limitation, the implicit Beam–Warming method with a subiteration strategy is incorporated to solve the low magnetic Reynolds number form of the governing equations. The k–ϵ equations are also integrated implicitly in time but are loosely coupled to the flow equations. This loose coupling considerably reduces the expense of computing the flux Jacobians.

The magnetogasdynamic equations resolve the flow within the domain, but boundary conditions must be specified to define the flow conditions along the computational boundary. For these simulations, the inflow boundary incorporated a supersonic inflow boundary condition, in which all variables at inlet were set to a constant value. No-slip boundary conditions were enforced along the tunnel walls, with the wall temperature limited to a peak of 2000 K. In addition, a zero normal pressure gradient was applied along the wall. Because the nominal flow was supersonic everywhere except in the small, subsonic portion of the boundary layers, the outflow boundary was set to supersonic extrapolation from the domain.

C. Control Volume Approach and Performance Analysis

The control volume (CV) formulation of the governing equations of motion lends itself to the determination of system-level interactions and overall performance. This form is conducive to postprocessing the highly 3-D, quasi-steady CFD flowfield solution and reducing it to a form better suited for evaluating impacts on the overall engine cycle performance. The postprocessing approach is similar to that taken by many commercial scientific visualization products. These equations can be derived directly from the differential form of the equations by application of Reynolds's transport theorem for a fixed control volume [19]. Furthermore, if the flow properties can be assumed constant across the flow cross section, then the quasi-1-D approach reduces the flow to dependence on a single spatial coordinate. Even though the inlet flow considered here has a complex 3-D character, by taking area and volumetric averaging of the grid point flow properties, the quasi-1-D approach can provide reasonable, conservative results. Finally, two more assumptions are made to obtain the equations that follow: 1) a single CV average value for the thermochemical properties can be taken (e.g., γ, c_v, c_p, etc.), and 2) the flow is steady in the sense that the influence of any $\partial/\partial t$ terms is negligible with respect to the steady terms. With this in mind, the CV equation for mass conservation is given by Eq. (9). Similarly, the momentum conservation equations are given by Eqs. (10–12), and energy conservation is given by Eq. (13):

$$(\rho A u)_e - (\rho A u)_i = \dot{m}_e - \dot{m}_i = \sum \dot{m}_o \tag{9}$$

where the subscripts e, i, and o refer to the exit plane, inlet plane, and any mass flow through the other boundaries (e.g., cowl spillage, fuel), respectively:

$$F_x = -\dot{m}_i u_i + \dot{m}_e u_e + \sum \dot{m}_o u_o + p_e A_e - p_i A_i \tag{10}$$

$$F_y = -\dot{m}_i v_i + \dot{m}_e v_e + \sum \dot{m}_o v_o \tag{11}$$

$$F_z = -\dot{m}_i w_i + \dot{m}_e w_e + \sum \dot{m}_o w_o \tag{12}$$

where the force components F_x, F_y, and F_z represent the total forces acting on the CV other than the inlet and exit boundaries, including those due to the Lorentz force, if present:

$$\frac{\mathrm{d}E}{\mathrm{d}t} = \dot{Q}_{\mathrm{ht}} + \dot{W}_{\mathrm{EM}} = \dot{m}_e\left(h_e + \frac{V_e^2}{2}\right) - \dot{m}_i\left(h_i + \frac{V_i^2}{2}\right) + \sum \dot{m}_o\left(h_o + \frac{V_o^2}{2}\right) \tag{13}$$

where $\dot{W}_{\mathrm{EM}}$ is the electromagnetic interaction term, defined in Eq. (3) as $\boldsymbol{E}\cdot\boldsymbol{j}$. This term can be further broken down into the algebraic sum of the work done on the control volume by the Lorentz force and the Joulean dissipation. The final result is given by Eq. (14). Note that, by convention, the rate of heat energy crossing the CV boundary in Eq. (13), $\dot{Q}_{\mathrm{ht}}$, is considered positive for heat entering the control volume:

$$\dot{W}_{\mathrm{EM}} = \boldsymbol{E}\cdot\boldsymbol{j} = \frac{|\boldsymbol{j}|^2}{\sigma} + \boldsymbol{V}\cdot(\boldsymbol{j}\times\boldsymbol{B}) \tag{14}$$

Four measures commonly used to describe inlet diffuser performance include the total pressure ratio π_c, the kinetic energy efficiency η_{KE}, the dimensionless entropy increase $\Delta s/C_p$, and the adiabatic compression efficiency η_c [20]. π_c and $\Delta s/C_p$ both rely on constant (or averaged) thermochemical properties to obtain analytical expressions from the solution of Gibbs's equation. Thus, although these measures by themselves will lose some accuracy for the high stagnation enthalpy flows that characterize the scramjet flowpath, they remain useful in determining trends when varying flow parameters. These two performance measures are given by Eqs. (15) and (16):

$$\pi_c = \frac{p_{t,e}}{p_{t,i}} = \frac{p_e}{p_i}\left\{\frac{1+[(\gamma-1)/2]M_e^2}{1+[(\gamma-1)/2]M_i^2}\right\}^{\frac{\gamma}{\gamma-1}} \tag{15}$$

$$\frac{\Delta s}{C_p} = \ell_n\left(\frac{T_e}{T_i}\right) - \frac{\gamma-1}{\gamma}\ell_n\left(\frac{p_e}{p_i}\right) \tag{16}$$

η_{KE} and η_c are both referenced to the freestream static conditions and thus are generally preferred for this type of flow. η_{KE} [Eq. (17)] is defined as the ratio of the square of the velocity the exit flow would achieve if isentropically expanded to freestream conditions to the square of the freestream velocity. Similarly, η_c [Eq. (18)] is the ratio of the isentropic change in enthalpy to the actual change in enthalpy, when both changes are referenced to the same change in static pressure:

$$\eta_{\mathrm{KE}} = \frac{V_e^2}{V_i^2} + \frac{2C_pT_e}{V_i^2}\left[1 - \left(\frac{p_i}{p_e}\right)^{\frac{\gamma-1}{\gamma}}\right] \tag{17}$$

$$\eta_c \doteq \frac{h_e - h_x}{h_e - h_i} \tag{18}$$

where the subscript x denotes the conditions that would exist upon an isentropic return to freestream from the given starting condition.

In addition, there is an additional performance measure commonly encountered when examining MGD flows. The enthalpy extraction/addition ratio or η_g is simply the ratio of the change in stagnation enthalpy across the MGD region to the value at the beginning of the MGD region [21,22]. To obtain a simpler analytical model, total enthalpy is often assumed conserved aside from the EM interaction due to the MGD device. However, as applied to this research, η_g includes not only the enthalpy change due to this EM interaction but also the change due to any other effects (e.g., geometric compression, heat of combustion). Because of this it may be difficult or impossible to separate out the EM contribution, especially when multiple factors are acting synergistically. Therefore, η_g is best viewed relative to similar flows as is done, for example, in the comparisons presented in this paper.

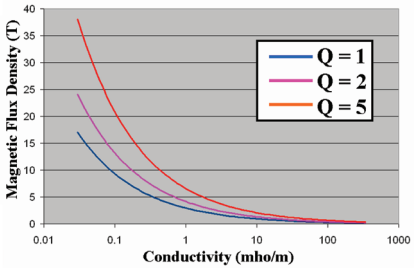

Fig. 1 Magnetic field requirements for varying Q, σ.

D. Approximating the Nonequilibrium Ionization with a Simplified Electron Beam Model

As presented in previous work [7], results from a quasi-1-D design tool were scaled to meet the mission requirements of a Mach 10 vehicle with 10,000 mile range. A design point dynamic pressure of 1000 lb_f/ft^2 was chosen, resulting in freestream conditions of $P_0 = 684$ Pa, $T_0 = 233$ K, $V_0 = 3060$ m/s, and $\rho_0 = 0.01022$ kg/m^3. Combining these with the leading edge width reference length of 3.602 m meant that $\sigma B^2 \approx 8.684Q$ or a maximum of 43.4 for $Q = 5$. Although large, these values are consistent with other proposed values [1,6]. Figure 1 presents the required magnetic field for a given value of conductivity at the values of Q used. By way of comparison, the natural conductivity of air at the freestream conditions has been shown to be on the order of 10^{-12} mho/m [23], implying that some form of nonequilibrium ionization is required to substantially reduce the required magnetic field. In fact, at these freestream conditions even the 0.1 mho/m values recently reported by Nishihara et al. [24] would require magnetic fluxes in on the order of 10 T.

The computational code as currently implemented does not specify an ionization method, but rather depends on the interaction parameter Q and the spatial distribution of the nondimensionalized electromagnetic field quantities to solve the coupled equations. However, with this research, a first-order approximation of the average magnitudes of σ_0 and B_0 is presented, as well as the required ionization power P_{ion} and generated electrical power P_{gen}. To accomplish this, a model to approximate the ionization was needed that could be adapted to the results generated by the existing 3-D computational code. Based on the wealth of previous work done by many in the field, it was decided the electron beam model provided a realistic approach to approximating the nonequilibrium ionization that could be readily adapted to the existing computational method. Specifically, the model of Kuranov and Sheikin [22,25,26] was used to determine the power spent on ionizing a unit volume of air, q_i, as given by Eq. (19), where $j_b \approx 1.0$ mA [27] is the electron beam current, e is the electron charge, ρ is the flow density and $Y(E_b) = 7.567$ MeV $\cdot$ cm^2/gm is the electron stopping power as a function of the electron energy. This last quantity was taken from tabulated data for dry air with an electron energy of $E_b = 30$ keV [28]:

$$q_i = (j_b/e)\rho Y(E_b) \tag{19}$$

The resulting conductivity is found from Eq. (20), where m_e is the electron mass, $k_e = 2 \times 10^{-8}$ cm^3/s is the electron scattering constant [29], and n_e/N is the ionization fraction, which has been shown to correlate well to the form given by Eq. (21) [25]. The number density N can be related to the density by $N = (\frac{RN_A}{R_u})\rho$, where R is the specific gas constant, R_u is the universal gas constant, and N_A is Avogadro's number:

$$\sigma = \frac{e^2}{m_e k_e}\left(\frac{n_e}{N}\right) \tag{20}$$

$$\frac{n_e}{N} = 1.17 \times 10^{-5} \cdot \left(10^{34}\frac{q_i}{N^2}\right)^{0.6} \tag{21}$$

Having a value of q_i and σ at each point, it is a simple matter to integrate over the plasma volume defined by the modifed Gaussian to arrive at P_{ion} and an overall mean value for σ_0. Then Eq. (22) is used to obtain a corresponding value for the mean magnetic flux density, where the asterisked quantities are the nondimensional values produced by the computational code. In a similar manner, the electrical power generated is simply found by integrating Eq. (23) over the plasma volume:

$$(\sigma B^2)_0 = (\sigma^* B^{*^2})\left(\frac{\rho V}{L}\right)_0 Q \tag{22}$$

$$P_{\text{gen}} = \iiint (\bar{j} \cdot \bar{E})\, \text{d(Vol)} \tag{23}$$

III. Improving Engine Performance by Application of Localized Inlet Flow Control

A. Baseline Engine Inlet

A wide assortment of techniques was implemented to create the inlet geometry shown in Fig. 2 [7]. The external–internal compression inlet performed marginally well insofar as it increased the mean static pressure to $57P_0$ at the inlet throat while limiting the static temperature rise to $5.1T_0$ as seen in Fig. 3b. (Recall from Sec. II.D that $P_0 = 684$ Pa and $T_0 = 233$ K.) However, this result was 23% below the minimum desired combustor inlet pressures of 1/2 atm, an outcome directly attributable to the inability of the quasi-1-D, inviscid inlet analysis to account for the 3-D effects discussed in this subsection. A review of Fig. 3b reveals that the local cross-sectional average of Mach number decreased fairly uniformly through the inlet from the reference value of $M_0 = 10$ to an inlet throat value of $M = 3.81$. This value at the throat is still higher than the Mach 1–3 range desired for a scramjet combustor, providing an opportunity for improvement through the use of MGD interaction. In addition, Fig. 3b shows the axial velocity experienced a substantial decrease in the vicinity of a large separation region downstream of the cowl shoulder. This separation region, which also caused the localized temperature spike at $x = 17.25$ m in Fig. 3a, is discussed in greater detail later in this paper. It was also a contributing factor to the baseline heat transfer of 69.6 MW out of the inlet walls. Regarding overall inlet performance and efficiency, a force balance using Eqs. (10–12) revealed a baseline drag of 86 kN, lift of −67 kN, and yaw of 870 N. The negative lift, or down force, was due to a mass flow spillage at the cowl lip, which is described in the following paragraph. Because the computational domain did not model the external flow around the cowl, it is not certain how much this down force would contribute to the overall vehicle flowfield and force balance. Finally, the system efficiencies were given by $\pi_c = 0.1519$, $\eta_{\text{KE}} = 0.8868$, $\Delta s/C_p = 0.4827$, and $\eta_c = 0.7525$, as defined by Eqs. (15–18), respectively. The last result showed the inlet performed somewhat less efficiently than the nominal value of $\eta_c = 0.9$ used by Heiser and Pratt in their analysis [20], a fact that was attributable to three key inlet flow features.

First and foremost, 59 kg/s, or roughly 22%, of the freestream mass flow spilled at the bottom cowl lip, never entering the internal compression portion of the inlet. This spillage loss was a purely 3-D effect attributable to the sidewall interaction. The additional sidewall

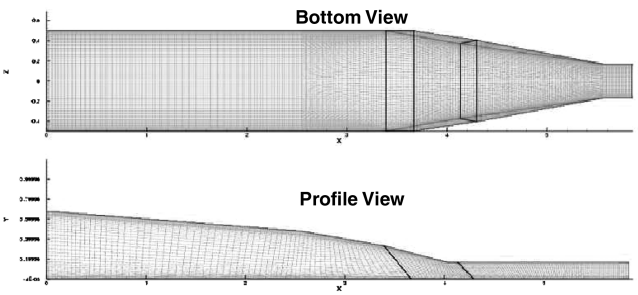

Fig. 2 Inlet grid normalized by freestream air capture width of 3.6 m.

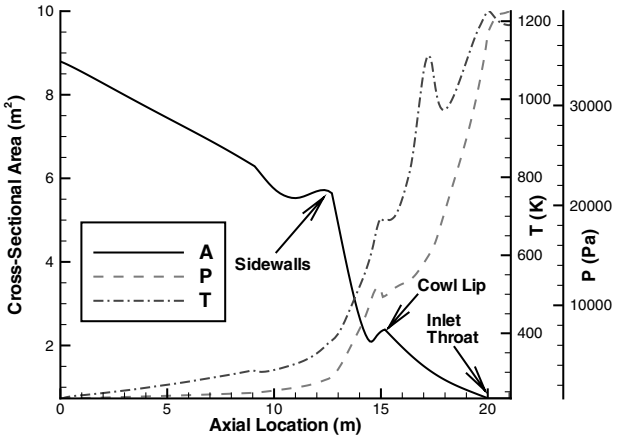

a) Mean values of static pressure and temperature within baseline inlet

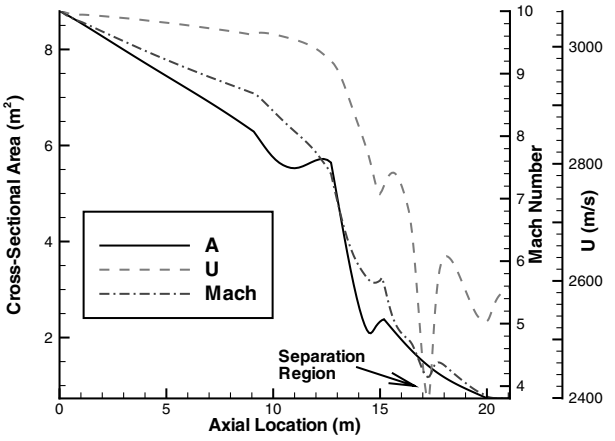

b) Mean values of mach number and normalized axial velocity within baseline inlet

Fig. 3 Baseline Mach 10 inlet geometry and selected flow properties.

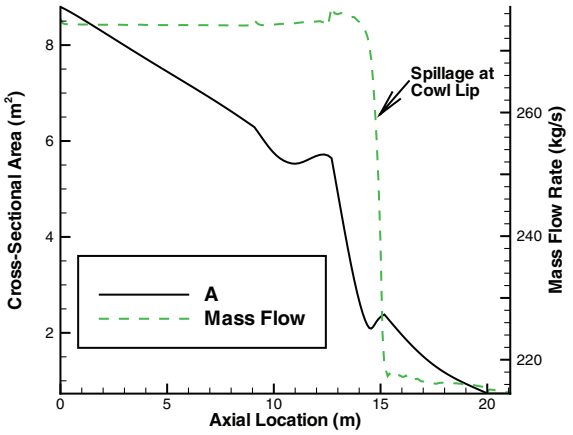

a) Mass flow rate

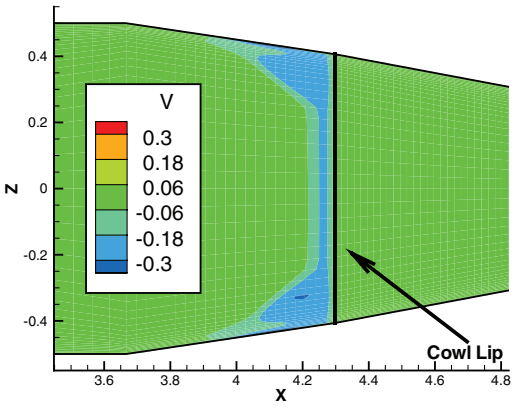

b) Normalized v-velocity contours demonstrating mass spillage in cowl lip vicinity

Fig. 4 Baseline inlet mass flow emphasizing cowl spillage.

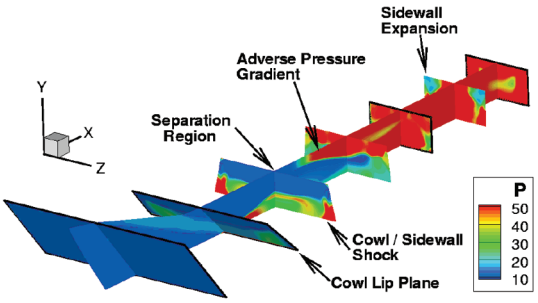

a) Pressure contours normalized by $P_0 = 687$Pa

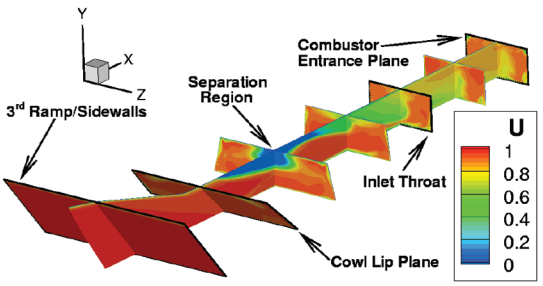

b) U-velocity contours normalized by $V_0 = 3060$m/s

Fig. 5 Baseline inlet flow emphasizing critical flow features.

compression caused the flow to seek pressure relief by turning downward, an effect previously documented by Holland and Perkins [5] and Holland [30]. This effect was clearly visible in Fig. 4a by the sharp decrease in mass flow rate at the cowl lip and in Fig. 4b by the increase in a negative v-velocity component near the cowl. Normally, this spillage could be countered by moving the cowl lip forward; however, the pressure relief is a desired effect for engine starting, which would occur at lower Mach numbers and higher pressures. Therefore, although it was not needed for the cruise test conditions examined in this research, this geometric feature was kept to improve the realism of the overall design.

Second, large areas of expanded flow developed downstream of the inlet shoulder (opposite of the cowl lip on the bodyside) and at the inlet throat. These expansions are clearly visible in Fig. 5a as the blue-shaded, low-pressure regions. Note that the pressure contours in this figure have been normalized by $P_0 = 684$ Pa. The pitch-plane expansion at the cowl shoulder was particularly detrimental to the compression efficiency as a large region of the bodyside flow returned to nearly freestream pressure conditions just before interacting with the shock reflected from the cowl lip. This interaction created a separation zone as shown in Fig. 5b, fairly symmetric about the k midplane, due to the severe adverse pressure

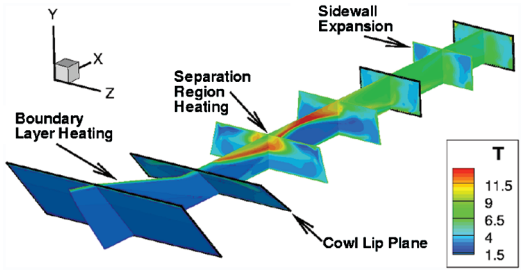

Fig. 6 Temperature contours in baseline inlet normalized by $T_0 = 233$ K.

gradient formed where the cowl lip shock reflected off of the bodyside and was met by the low-pressure, high-velocity expanded flow around the shoulder. The high pressure tended to reverse the flow in the vicinity of the boundary layer and propagate the pressure gradient upstream of the actual shock impingement until equilibrium was reached. This expansion–separation caused an estimated loss of nearly 10 kPa in the mean pressure at the inlet throat ($x \sim 20$ m in Fig. 3) and a significant amount of heating due to the locally stagnating flow, as seen in the temperature contours of Fig. 6. A further sidewall expansion into the isolator resulted in an additional 3 kPa mean pressure loss.

Finally, vortical structures, similar to the ones reported by Gaitonde [6], were observed from just downstream of the third pitch-plane ramp (Fig. 7a) through the rest of the inlet (Fig. 7b). These vortices were due primarily to the 3-D, viscous interaction brought about by the corner flows. This feature was enhanced by the sidewall compression shocks intersecting with those due to the pitch-plane compression. The net effect was an increase in the inlet total pressure loss and entropy rise and a decrease in overall flow momentum and compression efficiency.

B. Overview of the MGD Parameter Study

We raise the question as to whether MGD can be applied in this situation to mitigate or prevent the formation of the separation zone, improving the overall inlet flowfield and specifically the flow entering the combustor. Two concepts were considered. The first concept used an MGD generator to increase pressure, especially in the cowl shoulder region, to better match that of the reflected shock. Alternatively, an MGD accelerator was considered to increase flow momentum in the portions of the inlet subject to locally expanding flow. This was hypothesized to be especially helpful when focused on the low-momentum boundary layer, where the adverse pressure gradient initiated flow separation.

Thirty-two different cases of localized EM fields and corresponding regions of specified conductivity were applied immediately downstream of the cowl shoulder on the bodyside in an effort to mitigate this performance loss. In all cases, the $\boldsymbol{B}$ field was uniform and aligned in the $+Y$ direction, and the $\boldsymbol{E}$ field was likewise uniform but aligned in the $-Z$ direction. Four different distributions for σ were explored; the two primary cases, referred to as case 1 and case 2, respectively, appear as the contoured regions in Figs. 8a and 8b. These two cases differed only in the axial extent of the plasma volume. For both cases, an additional subcase was explored wherein the conductivity was centered just outside the boundary layer as in Fig. 8c. This subcase simulated an electron beam with the maximum conductivity centered several centimeters from the wall. The conduction current density $\boldsymbol{j}$ was given by Ohm's law in Eq. (4) and was therefore in the $\pm Z$ direction, depending on the magnitude of the nondimensional load factor k, which was tested at values of 0.0, 0.7, 1.0, and 1.3. The Lorentz force as given by $\boldsymbol{j} \times \boldsymbol{B}$ was then in the $-X$ direction (or decelerating the flow) for $k < 1$ and in the $+X$ direction (accelerating) for $k > 1$. Finally, interaction parameters of $Q = 1$ and 5 were examined at the prescribed freestream flight conditions to gauge the effect of increasing $\boldsymbol{B}$.

C. Results from Conductivity Case 1

The addition of EM fields had limited effect on the outflow properties, with the exception of the $k = 0$ parameter cases, which resulted in extreme dissipative heating. This heating increased average temperatures 24 and 77% above baseline for $Q = 1$ and $Q = 5$, respectively. This was due to the fact that, with no external load applied, all of the extracted electrical energy must dissipate within the flow itself. The accelerator case, $k = 1.3$, $Q = 5$, also experienced additional heating, but to a lesser extent, due to the deposition of additional external energy. For this case, the $Q = 5$ interaction elevated the temperature 18% above baseline. For the remaining parameters, Mach number, γ, and temperature were virtually unchanged from the baseline case. The pressure showed the same trends as temperature but to a lesser degree. For $k = 0$, pressures increased above baseline by 12 and 54%, and for $k = 1.3$, $Q = 5$, the pressure increase was 16%. As Fig. 9 shows, only the $k = 0.0$, $Q = 5$ case exhibited substantial gains in pressure upstream of the inlet throat, due to the EM interaction upstream of the separation region. The expansion at the inlet throat, however, had a dominant influence on the flow, drastically reducing any potential pressure increases.

With the exception of $k = 0$ and $k = 1.3$, $Q = 5$, the efficiencies for cases 1 and 1B were only marginally impacted as seen in Fig. 10. (Note: in these comparison bar charts to follow, the numbers 1, 1B, etc., refer to the conductivity profile, whereas "kX.X" refers to the load factor and Q the interaction parameter used.) The greatest impact on efficiency was with $k = 0$, $Q = 5$, where π_c was reduced to 3% of the freestream value and η_C decreased by 6.7% with respect to baseline. $\Delta s/C_p$ and η_{KE} were similarly impacted with an increase of 49% and decrease of 4%, respectively, for this case. In an interesting result, it was noted that the largest increase in η_{KE}, 8% above baseline, occurred for $k = 1.3$, $Q = 5$. This makes sense from the perspective that energy external to the inlet was added in a

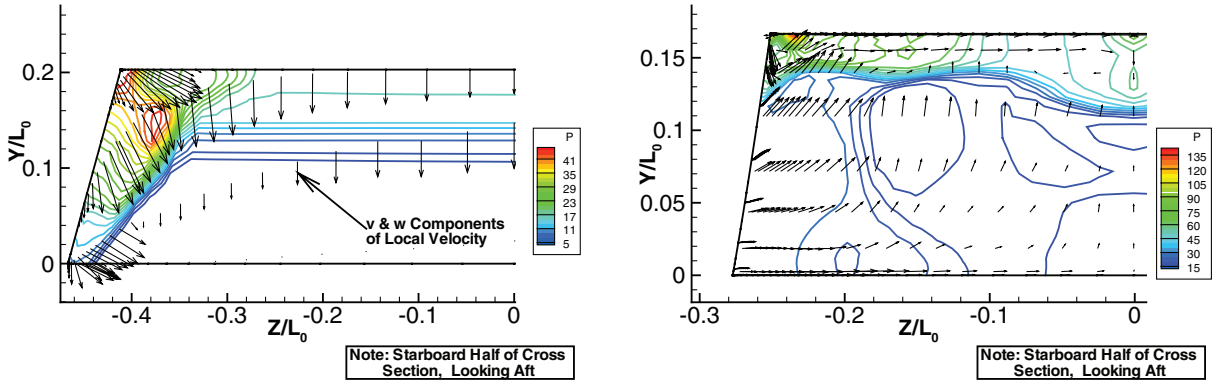

a) Between 3rd pitch ramp and cowl plane, x=14.0m

b) Midway between cowl and throat, x=18.0m

Fig. 7 Selected cross sections of baseline inlet with pressure contours normalized by $P_0 = 684$ Pa and velocity vectors that demonstrate presence of 3-D vortical flow structures.

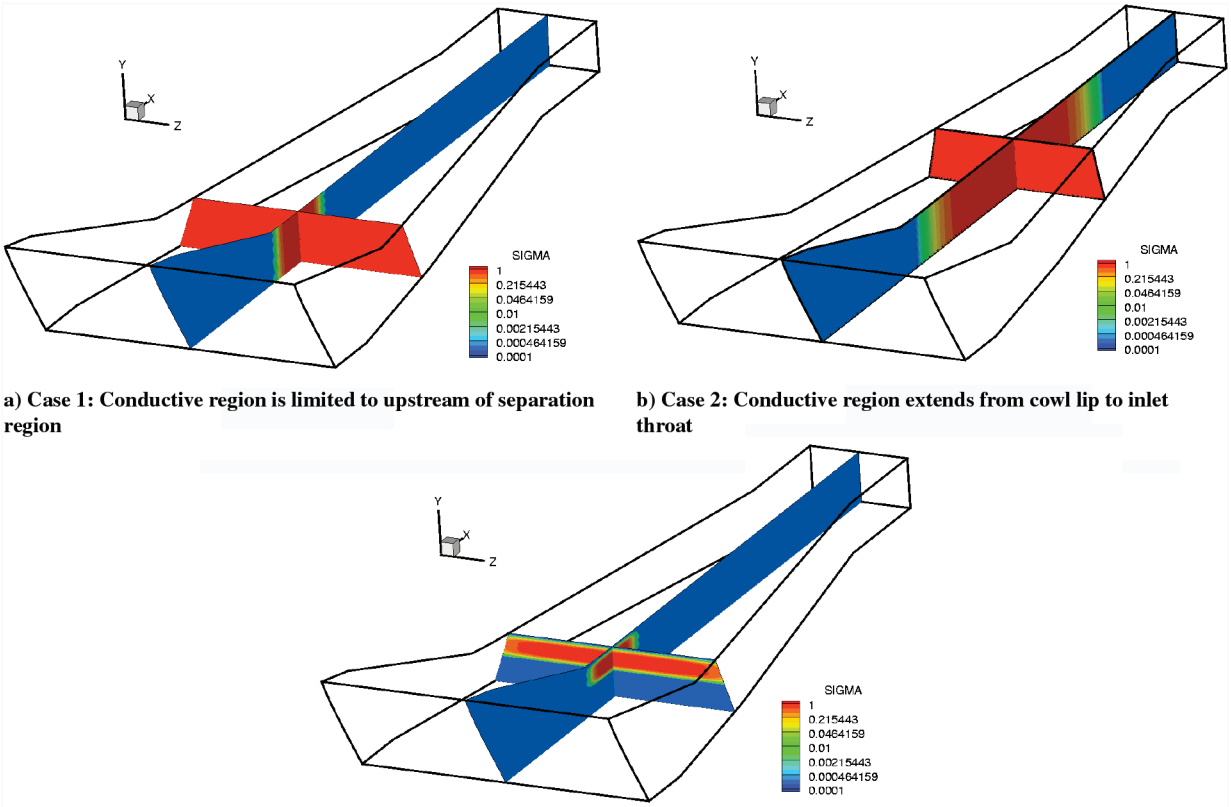

a) Case 1: Conductive region is limited to upstream of separation region

b) Case 2: Conductive region extends from cowl lip to inlet throat

c) Case 1B: Conductive region centered outside of boundary layer

Fig. 8 Full cross section nondimensional conductivity (SIGMA) profiles in inlet.

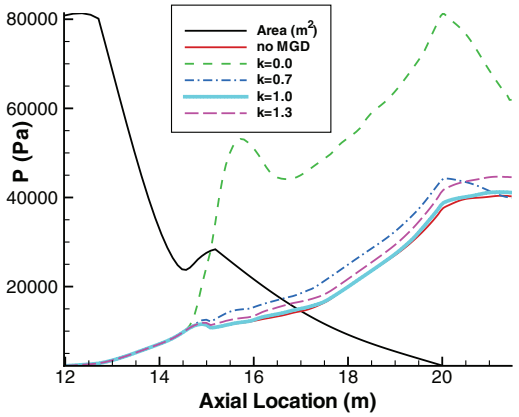

Fig. 9 Mean inlet pressure for case 1 with varying k and $Q = 5$.

manner that increased the kinetic energy and thus the momentum in the inlet, as desired.

Following the same trend, Fig. 11 reveals that the parameter $k = 0$, $Q = 5$ had the greatest impact on drag at 158% greater than baseline, corresponding to the highest Lorentz force at −111.0 kN. For constant k, higher Q meant higher Lorentz force as expected. Also, as one would expect, increasing the departure from $k = 1$ increased the Lorentz force. This was readily apparent in the overall axial force imposed on the inlet. At $k = 1$, the interaction was minimal and the net drag was actually reduced 7% below baseline. The biggest decrease in drag occurred, as expected, for $k = 1.3$, where the positive Lorentz force for $Q = 1$ was 10 kN and for $Q = 5$ was 42 kN. This resulted in drag reductions of 16 and 56%, respectively, with respect to baseline. In an unexpected result, it was observed that as k went to zero there was a significant increase in mass flow spillage out of the inlet at the cowl lip. This was unique to case 1 and was due to the full cross section conductivity profile that extended upstream of the cowl lip plane. In effect, the Lorentz force allowed the bypass of an additional 18 kg/s of air around the cowl. This additional mass flow slightly mitigated the drag increase induced by the Lorentz force. In effect, this produced a thrust, just as it would in a bypass turbofan engine. This additional spillage was easily visualized by comparing the increased thickness of the spillage contours for the $k = 0$, $Q = 5$ parameters as seen in Fig. 12 to those of the inlet without MGD as seen in Fig. 4b.

As discussed in Sec. II.C, the time rate of energy change in the control volume, dE/dt, is equal to the heat transfer rate through the CV, $\dot{Q}_{ht}$, plus the EM energy interaction, $\dot{W}_{EM} = \boldsymbol{E} \cdot \boldsymbol{j}$. All of the EM cases deposit some energy into the flow through dissipation, with the amount increasing as k departs from a value of 1. Interestingly, although all cases had a net heat transfer out of the CV, some of the MGD cases exhibited less overall heat transfer than the baseline case. With the exception of $k = 0$, all of the $Q = 1$ cases had 5–17% less as seen in Fig. 13. These decreases were attributed to the fact that the stagnation region due to separated flow moved slightly farther away from the wall, while at the same time the low interaction of $Q = 1$ contributed only 25–30% of its $Q = 5$ amount. A closeup examination of the separation region revealed this unexpected result, a result that would later become more significant in plasmas limited to the near-wall region. From Figs. 14a and 14b it was evident the EM cases caused the separation region to actually grow compared to the baseline case. However, this same effect caused the stagnant flow to also move away from the wall, creating a buffer zone of relatively lower temperatures next to the wall as seen in Figs. 14c and 14d. This change in the heat distribution decreased the wall heat transfer by a small amount.

Conversely, the maximum value of 180 MW (or 159% above baseline) occurred for $k = 0$, $Q = 5$. $k = 0.7$ and 1.3 cases inject roughly the same amount of dissipation into the flow on the order of 9 and 34 MW for $Q = 1$ and 5, respectively. However, whereas dissipation constituted roughly 40% of the total $\dot{W}_{EM}$ for $k = 0.7$, it comprised only 27% of the total for $k = 1.3$. Therefore, as an overall measure, the generator case at $Q = 5$ reflected an overall greater heat transfer rate through the CV boundaries. The $k = 1$ cases put the least amount of dissipation into the system (on the order of 1.2–3.6 MW)

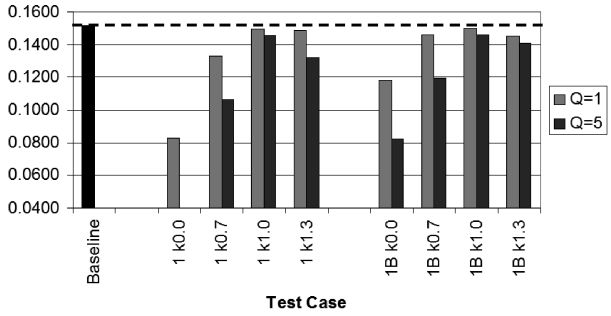

a) Total pressure ratio

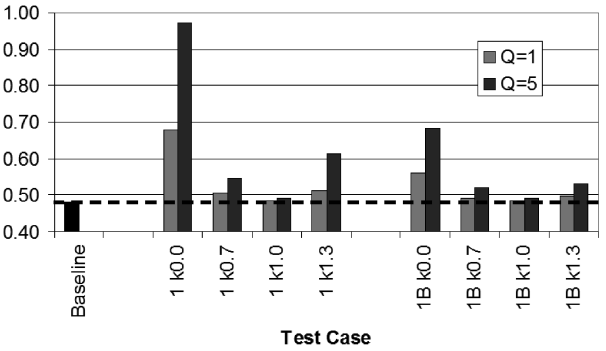

b) Dimensionless entropy rise

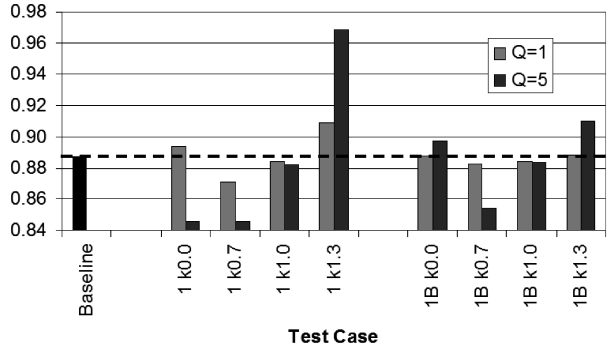

c) KE efficiency

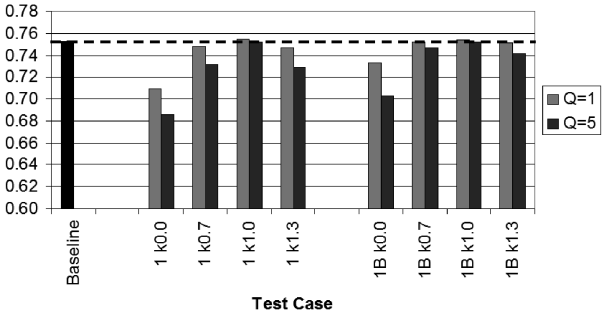

d) Adiabatic compression efficiency

Fig. 10 Inlet efficiency metrics for cases 1 and 1B.

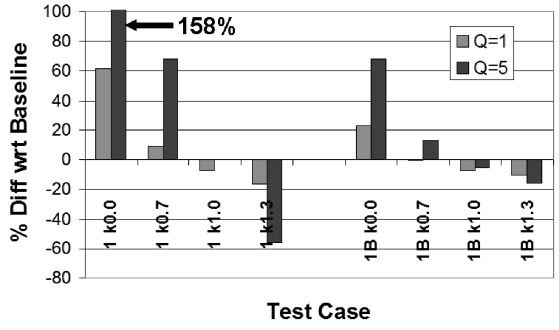

Fig. 11 Comparison of net inlet drag for conductivity case 1.

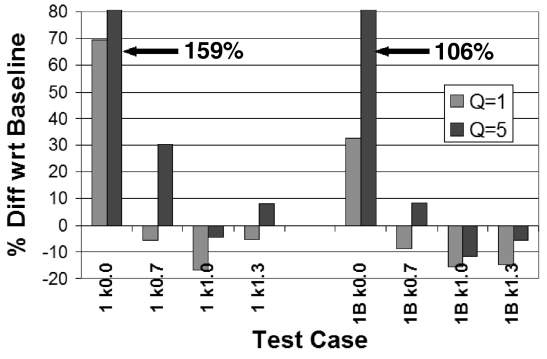

Fig. 13 Comparison of normalized heat transfer for conductivity cases 1 and 1B.

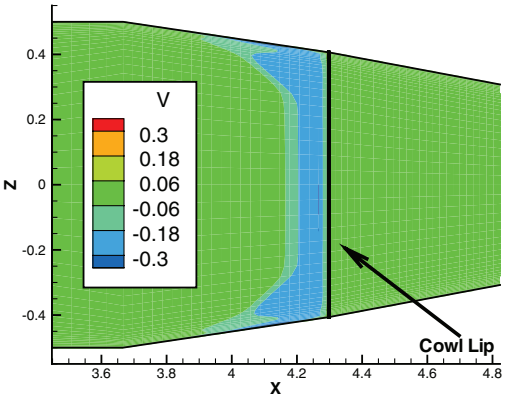

Fig. 12 v/V_0 contours demonstrating additional cowl lip mass spillage for $k = 0.0$, $Q = 5$.

because $k = 1$ represents the open circuit case where the conduction current is approximately zero. Joulean dissipation varies directly with the current, thus the lower the current (i.e., k closer to 1) the less the flow is heated.

Regarding the ionization model, the conductivity region filled approximately 3.0 m^3 with values of σ ranging between 0.63 and 0.86 mho/m. B-fields were on the order of 3.3 T for $Q = 1$ and 7–8 T for $Q = 5$. Net power generation was simply the difference between the generated electric power P_{gen} and the ionization power P_{ion}, as defined in Sec. II.D. Referring to Fig. 15, only the $k = 0.7$ cases demonstrated a meaningful net power generation with 18 MW for $Q = 1$ and 82 MW for $Q = 5$. The required power for ionization was on the order of 1.3–1.5 MW for all cases. The enthalpy extraction ratio η_g, defined in Sec. II.C, was typically in the range of 10–20% but reached a maximum of 31% for the $k = 0.0$, $Q = 5$ generator, as shown in Fig. 16. The $k = 1.3$, $Q = 5$ accelerator actually increased the enthalpy by 1%. Recall from Sec. II.C, however, that this measure includes changes due to both EM interaction as well as geometric compression.

D. Results from Conductivity Case 1B

In contrast to case 1, we limited the conductivity for this case to the near-wall region of the cowl shoulder. Case 1B, with a plasma volume of 1.44 m^3, more accurately simulated an electron beam ionization source with the maximum conductivity centered several centimeters from the wall and then falling off rapidly in the direction normal to the wall. As in case 1, the addition of EM fields had a small, but noticeable, effect on the outflow properties, primarily with

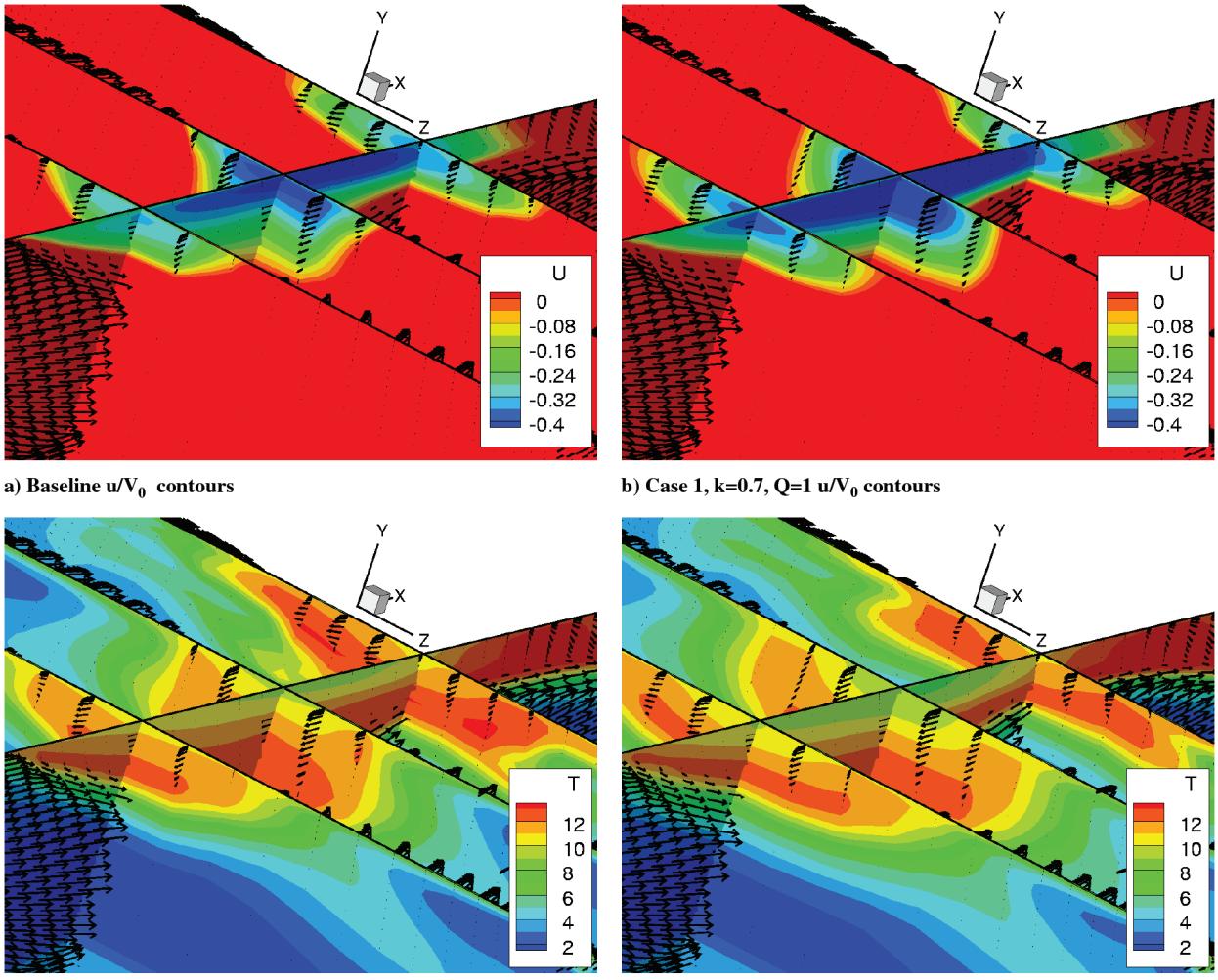

a) Baseline u/V_0 contours

b) Case 1, k=0.7, Q=1 u/V_0 contours

c) Baseline T/T_0 contours

d) Case 1, k=0.7, Q=1 T/T_0 contours

Fig. 14 Impact of EM interaction on inlet separation region, in which arrows represent the normalized local velocity vector.

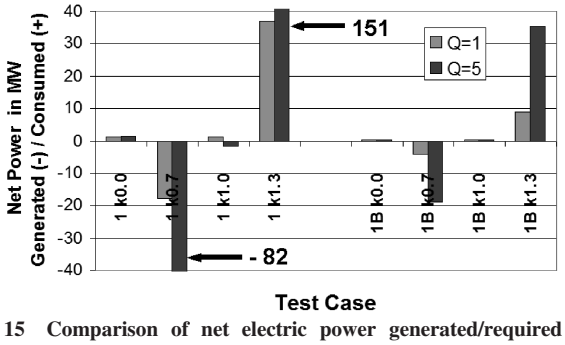

Fig. 15 Comparison of net electric power generated/required for conductivity cases 1 and 1B.

respect to temperature and pressure increases. However, the magnitude of these changes was much less than for the same EM interaction applied to case 1. For example, the greatest change in exit pressure occurred for $k = 0.7$, $Q = 5$ and amounted to a 6.7% increase above the baseline inlet. This was expected, in light of case 1, as the interaction region for 1B was only 48% of case 1. However, forces, heat transfer and EM terms did vary for differing parameters as applied to case 1B, as discussed in this section.

Referring back to Fig. 11, drag varied from 16% less than baseline for the $Q = 5$ accelerator to 68% more than baseline for the $k = 0.0$, $Q = 5$ parameters. Overall, these numbers reflect the same trends as in case 1 but typically at magnitudes of 1/3 to 2/3 of their case 1 counterparts. As with case 1, for a given k, there was an obvious change in drag for increased Q, due to the increasing magnitude of the Lorentz force. The near-wall conductivity region (being limited to the opposite side of the flowfield away from the cowl lip) did not induce any additional mass spillage. Therefore, there was no contribution to thrust due to bypassed air flow as seen in case 1. Regarding heating, all of the EM cases deposited energy into the flow through dissipation, but typically in less amounts than for case 1. The heat transfer rates out of the control volume reflect this (Fig. 13). For case 1B, the minimum and maximum values for the heating, $\dot{Q}_{\text{ht}}$, were 59 and 143 MW. The same trends as for case 1 were seen in that $k = 0$ by far produced the most Joulean dissipation, $k = 1.3$ and $k = 0.7$ were comparable, and $k = 1.0$ produced the least amount. It was interesting to note that at $Q = 1$, cases 1 and 1B had very similar values of wall heating for corresponding k values (with the exception

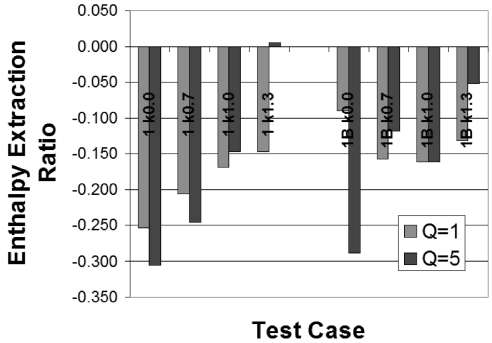

Fig. 16 Comparison of enthalpy extraction/addition for conductivity cases 1 and 1B.

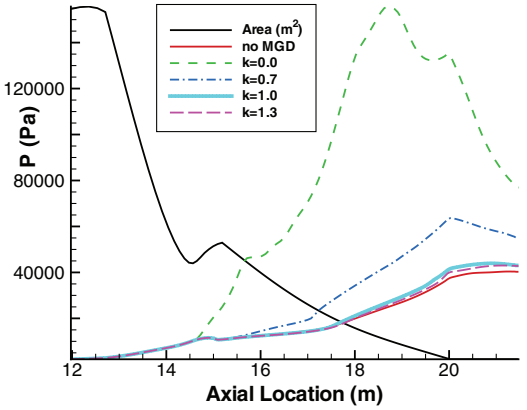

Fig. 17 Mean inlet pressure for case 2 with varying k and $Q = 5$.

of the $k = 0$ parameter). This fact demonstrated that the placement of EM interaction near the wall was the driving factor in determining the wall heat transfer. Overall, the targeted application of conductivity appeared to be a relatively efficient method of limiting the overall drag increase due to Lorentz force. However, further work is recommended to determine the optimum distance off the wall to target the electron beam ionization to minimize the additional wall heat load while retaining the drag reduction benefit.

Conductivity for these cases was somewhat higher than in case 1, ranging between 0.85 and 0.97 mho/m. This was because densities near the wall were less than in the core flow, which from Eqs. (19–21) implied conductivity should be higher as $\sigma \propto 1/\sqrt{\rho}$. By the same reasoning, the required P_{ion} per unit volume was also less than for case 1. Magnetic fields were on the order of 3 T for $Q = 1$ and 6.5–7 T for $Q = 5$. Once again, as seen in Fig. 15, only the $k = 0.7$ MGD generator cases demonstrated a substantial net power generation after ionization. A net of 4.1 MW was produced for $Q = 1$ and 19 MW for $Q = 5$, which was 23% of that produced for the corresponding parameters applied to case 1. The required power for ionization was on the order of 0.5 MW for all cases. The enthalpy extraction ratios η_g were generally comparable to case 1, which in light of the differing volumes of the interaction region reveals that the effect of enthalpy extraction due to EM interaction is not as significant as other mechanisms such as wall heat transfer.

E. Summary of Conductivity Cases 1 and 1B

From this analysis, it appeared that neither of the control mechanisms presented in case 1 nor 1B were effective at significantly increasing the mean pressure at the outflow plane or improving efficiency. One exception to this conclusion regarding pressure for $k = 0.0$, $Q = 5$ must be made. However, even in this case the quasi-1-D plot of Fig. 9 revealed that any gains incurred from the EM interaction upstream of the separation region were substantially reduced by the sidewall expansion into the isolator at the inlet throat. Several notable improvements were observed, though. Placement of the EM interaction region near the wall was the most important factor in determining the wall heat transfer, and targeting the conductivity to this region did appear to be a relatively efficient method of limiting drag increases. However, these two conclusions together mean further work is needed to determine the optimum distance off the wall to target the electron beam ionization. Finally, the additional mass flow spillage caused by placing the interaction region near the cowl lip had a noticeable impact on the inlet flow. Although developing a mass flow rate active control system along the lines of Macheret et al.'s conceptual work [1] was beyond the scope of this work, this computational modeling serves as the first high-fidelity proof of this potential application.

F. Results from Conductivity Case 2

Case 2 continued the conductivity region downstream through the separation region until reaching the inlet throat as shown in Fig. 8b. This plasma was about 2.6 times the volume of the case 1 plasma, or

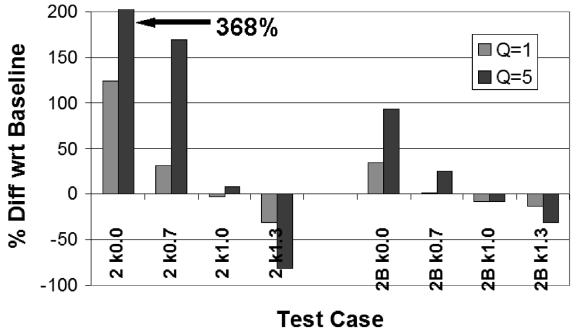

Fig. 18 Comparison of net inlet drag for conductivity cases 2 and 2B.

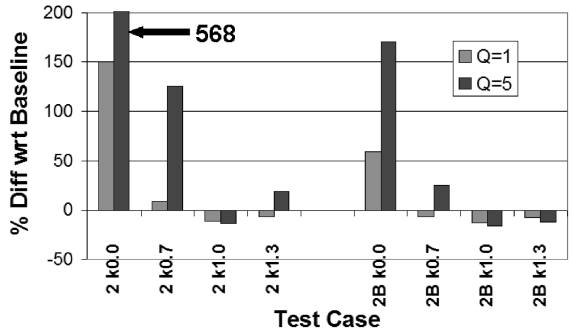

Fig. 19 Comparison of wall heat transfer for conductivity cases 2 and 2B.

7.59 m^3. Consequently, the impact to forces, heat transfer, and, in contrast to case 1, exit plane flow properties, was significant and varied greatly with the different parameters. For example, as shown by Fig. 17, the exit plane pressure was 30 kPa, or 74%, above the baseline case for $k = 0.0$, $Q = 5$. Other than the $k = 0.0$ parameter, $k = 0.7$ cases showed appreciable pressure increases of 18 and 25% for $Q = 1$ and 5, respectively. However, all of these pressure rises were accompanied by a large amount of dissipative heating, resulting in a maximum mean temperature of 3265 K for the $k = 0$, $Q = 5$ case. It was apparent from these results and a review of Figs. 9 and 17 that raising the pressure in the isolator was accomplished most effectively by modifying the sidewall expansion fans into the inlet throat.

Looking further at the drag forces and heating, the accelerator parameters of $k = 1.3$, $Q = 5$ reduced the net inlet drag to 16 kN (or 81% less than baseline), as shown in Fig. 18, but at the substantial cost of 240 MW of electrical power put into the system. Although all cases resulted in overall inlet drag, the $k = 1.3$, $Q = 1$ case likewise reduced the baseline value by 31%, at a cost of only 30% of the electrical power consumed at $Q = 5$. As k decreased (or Q increased for a given k), the drag increased, reaching a maximum value of −404 kN (a 368% increase with respect to baseline) for $k = 0$, $Q = 5$. This made sense in both respects as a decreasing k and/or increasing Q means an increasing Lorentz force in the negative axial direction. The increased mass flow spillage of case 1, and its effect on drag, was not seen with case 2 because, as discussed in Sec. III.C, only case 1 extended the MGD interaction region upstream of the cowl lip plane. Regarding $\dot{Q}_{\text{ht}}$ and the results presented in Fig. 19, all cases resulted in heat transfer out of the CV. Just as with case 1, small decreases were seen with respect to baseline for parameters that resulted in a relatively low level of EM interaction. As seen previously with case 1, increasing the EM energy interaction always results in increased dissipative losses, regardless of whether the device acts as a generator or an accelerator. The trend in heating was the same as for case 1 in that the greater the departure from $k = 1$, the higher the dissipation and subsequent heating. The peak value was an astounding 465 MW for the $k = 0$, $Q = 5$ case.

Finally, conductivity and B-field values for this case were comparable to those of case 1 because the density increased slowly through this portion of the inlet. Values of σ ranged between 0.51 and

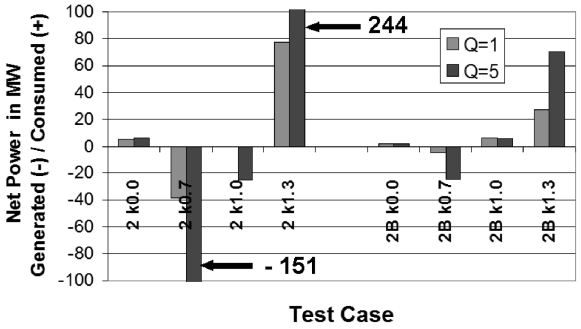

Fig. 20 Comparison of net electric power generated/required for conductivity cases 2 and 2B.

0.79 mho/m, and B-fields were on the order of 3.5 T for $Q = 1$ and 7.5–9.2 T for $Q = 5$. The $k = 0.7$ cases generated a net 39 MW and 151 MW of electrical power for Q = 1 and 5, respectively, as depicted in Fig. 20. In addition to the $k = 0.7$ cases, the $k = 1$, $Q = 5$ case demonstrated a net power generation after ionization of 25 MW. These large values of P_{gen} are important as, aside from the ionization power requirements, other electrical power requirements must be met. However, these considerations are beyond the scope of this modeling effort (e.g., electromagnet power supplies and control circuitry). With plasma volume 2.6 times greater than that of case 1, the required power for ionization was on the order of 4.1–6.3 MW for all cases. This was up to approximately 3–4 times the required P_{ion} of case 1, demonstrating that in light of the axially increasing inlet density, the per-unit volume cost of producing the plasma was approximately the same for both case 1 and 2.

G. Results from Conductivity Case 2B

Although not explicitly shown, in reference to Fig. 8, one can interpret case 2B as a combination of the near-wall profile of 1B extended axially to the same point as case 2. Case 2B had a plasma volume of 3.76 m^3. Focusing the EM interaction in the near-wall and especially the separated-flow region resulted in slight increases in the exit flow pressures and temperatures. Exit Mach numbers decreased by less than 10% with respect to baseline for all but the $k = 0$, $Q = 5$ case, which decreased by 20%. Efficiencies relative to the baseline inlet were similar to their case 1B counterparts as seen in Fig. 21. The decreases in efficiency measures were not as great as those for case 2 because of the smaller, targeted interaction region. Likewise, results from case 2B did not exhibit the adversely large heat loads and electrical power requirements seen in case 2.

For example, Table 1 compares the $k = 1.3$, $Q = 5$ accelerator parameters for cases 2 and 2B. Case 2B had significantly less EM work done, resulting in less heat generation and lower electrical power requirements. Of course, due to the inevitable Joulean dissipation, there was a measurable temperature rise in all instances as also reflected in Table 1. Though not shown in Table 1, the $k = 0$, $Q = 5$ parameters had the most negative impact to compression efficiency, with case 2B being 5.4% less efficient than baseline. Still, this was a marked improvement over the 9.9% lower efficiency for the same parameters applied to case 2.

The drag results for case 2B varied widely, but as seen in Fig. 18, it was a minimum of 31% less than baseline at $k = 1.3$, $Q = 5$. A maximum drag value of 94% greater than baseline was obtained for case 2B when $k = 0.0$, $Q = 5$. From Fig. 19, heat transfer out through the walls was a minimum for $k = 1.0$, $Q = 5$ with a value of 58 MW, 16% less than baseline. Maximum $\dot{Q}_{\text{ht}}$ corresponded to the $k = 0$, $Q = 5$ parameter (as in the other cases), having a specific value of 188 MW (177% above baseline). Trends for heating and drag followed the other cases. Conductivity was somewhat higher than in case 2, ranging between 0.77 and 0.98 mho/m. As with case 1B, B-fields were on the order of 3 T for $Q = 1$ and 6–7.5 T for $Q = 5$. Once again, Fig. 20 revealed that only the $k = 0.7$ cases demonstrated a net power generation after ionization with case 2B producing a net of 5 MW for $Q = 1$ and 24 MW for $Q = 5$. The required power for ionization was on the order of 1.6–1.8 MW for all cases. With reference to Fig. 21, the MGD accelerators for cases 2 and 2B showed marginal improvement in flow properties as well as significant drag reduction and increased η_{KE}. However, these cases also required a very large electrical power input. This detrimental factor was reduced to a great extent by localizing the plasma region to the near wall in case 2B, resulting in an electrical power requirement of 27 and 70 MW, for $Q = 1$ and $Q = 5$, respectively.

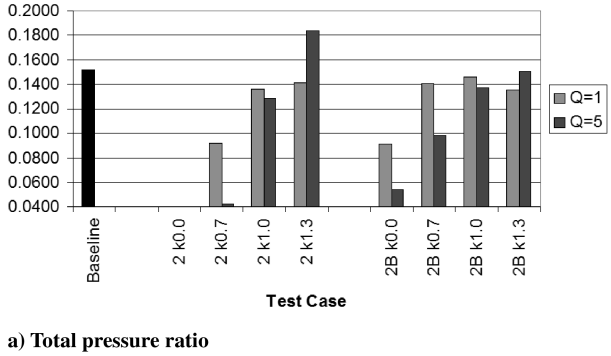

a) Total pressure ratio

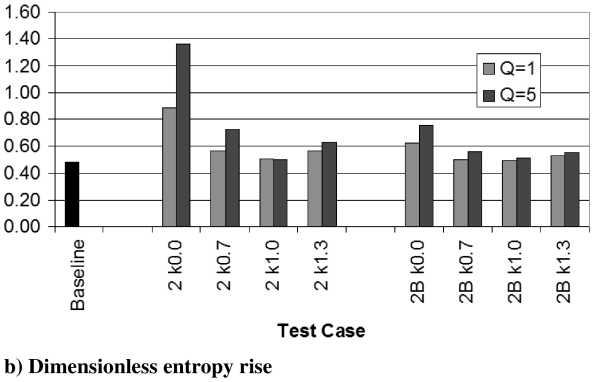

b) Dimensionless entropy rise

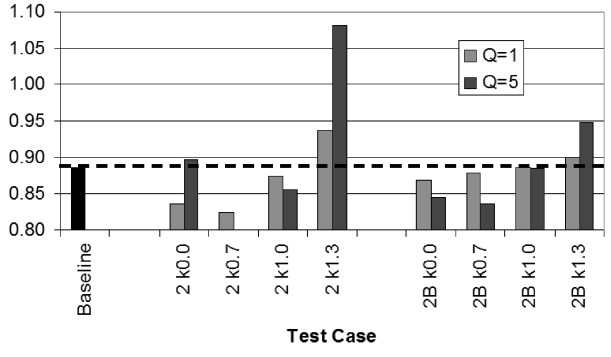

c) KE efficiency

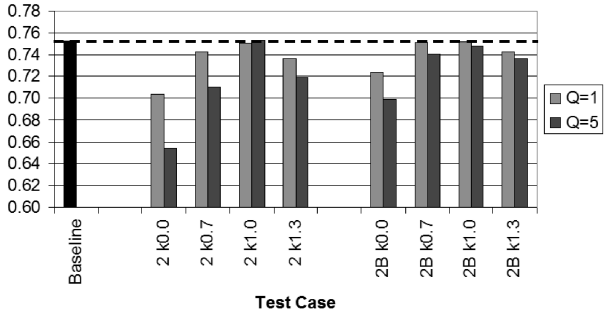

d) Adiabatic compression efficiency

Fig. 21 Inlet efficiency metrics for cases 2 and 2B.

Table 1 Selected results for MGD accelerators, $k = 1.3$, $Q = 5$

Property	Units	Case 2	Case 2B
p_e	kPa	42.8	41.8
T_e	K	1418	1316
Axial force	kN	−16.1	−60.1
Wall heat transfer, $\dot{Q}_{\text{ht}}$	MW	−82.9	−61.4
Net power	MW	244	70.0
Total pressure ratio, π_c	——	0.1838	0.1506
Nondimensional entropy rise, $\Delta s/C_p$	——	0.6241	0.5522
KE efficiency, η_{KE}	——	1.0805	0.9476
Adiabatic compression efficiency, η_c	——	0.7188	0.7357

IV. Conclusions

With respect to the specific application presented here, localized MGD flow control was marginally successful in mitigating the pressure losses due to the expansion around the cowl shoulder. The $k = 0.0$, $Q = 5$ parameter, in particular, can significantly raise the average inlet pressure. Yet, the penalty in terms of drag and heating excludes its consideration as a viable solution to the problem. All other parameters for cases 1 and 1B were not effective at significantly increasing the mean pressure at the outflow plane or improving the inlet efficiency. Gains incurred by these parameters from the EM interaction upstream of the separation region were all but negated by the sidewall expansion into the isolator at the inlet throat.

Placement of the EM interaction region near the wall was the most important factor in determining the wall heat transfer, and targeting the conductivity to this region did appear to be a relatively efficient method of limiting drag increases. However, further work is recommended to determine the optimum distance off the wall to target the electron beam ionization. Finally, with respect to case 1 only, the additional mass flow spillage caused by placing the interaction region near the cowl lip had a noticeable impact on the inlet flow. This computational model provided the first high-fidelity verification of the potential for using MGD to modulate the mass flow rate into a scramjet engine.

For the MGD generator cases of $k = 0.7$, meaningful electrical power generation was achieved. Although it only slightly increases the flow pressure into the isolator, MGD acceleration, particularly for case 2B, can efficiently reduce the net inlet drag. This was accomplished while minimizing the increase in heat transfer and decrease in overall efficiency measures, due primarily to increasing the flow momentum as it passed through the sidewall expansion into the inlet throat. Therefore, the use of an MGD accelerator to locally increase flow momentum was an effective approach to improve flow into the isolator of this scramjet model. Further, if the P_{ion} requirement is of prime consideration, limiting the ionized flow to the near-wall region is an acceptable compromise.

Acknowledgment

The views expressed in this article are those of the authors and do not reflect the official policy or position of the United States Air Force, the Department of Defense, or the U.S. Government.

References

[1] Macheret, S., Shneider, M., and Miles, R., "Magnetohydrodynamic Control of Hypersonic Flows and Scramjet Inlets Using Electron Beam Ionization," *AIAA Journal*, Vol. 40, No. 1, 2002, pp. 74–81.

[2] Macheret, S., Shneider, M., and Miles, R., "Scramjet Inlet Control by Off-Body Energy Addition: A Virtual Cowl," AIAA Paper 2003-0032, 2003.

[3] Macheret, S., Shneider, M., Van Wie, D., and Miles, R., "MHD Power Generation in Scramjet Engines in Conjunction with Inlet Control," AIAA Paper 2004-1197, 2004.

[4] Shneider, M., and Macheret, S., "Modeling of Plasma Virtual Shape Control of Ram/Scramjet Inlet and Isolator," AIAA Paper 2004-2662, 2004.

[5] Holland, S., and Perkins, J., "Contraction Ratio Effects in a Generic Three-Dimensional Sidewall Compression Scramjet Inlet: A Computational and Experimental Investigation," AIAA Paper 1991-1708, 1991.

[6] Gaitonde, D., "Three-Dimensional Flow-Through Scramjet Simulation with MGD Energy Bypass," AIAA Paper 2003-0172, 2003.

[7] Lindsey, M., McMullan, R., and Gaitonde, D., "Development of a Realistic 3-D Scramjet Flowpath for MGD Energy Bypass," AIAA Paper 2005-1178, 2005.

[8] Lindsey, M., and McMullan, R., "Computational Study of MGD Flow Control on a Flight-Scale Scramjet," AIAA Paper 2006-0371, 2006.

[9] Hughes, W., and Young, F., *The Electromagnetodynamics of Fluids*, John Wiley and Sons, New York, 1966.

[10] Sutton, G., and Sherman, A., *Engineering Magnetohydrodynamics*, McGraw–Hill, New York, 1965.

[11] Rosa, R., *Magnetohydrodynamic Energy Conversion*, McGraw–Hill, New York, 1968.

[12] D'Ambrosio, D., and Giordano, D., "Electromagnetic Fluid Dynamics for Aerospace Applications. Part 1: Classification and Critical Review of Physical Models," AIAA Paper 2004-2165, 2004.

[13] Gaitonde, D., "Development of a Solver for 3-D Non-Ideal Magnetogasdynamics," AIAA Paper 1999-3610, 1999.

[14] Gaitonde, D., and Poggie, J., "An Implicit Technique for 3-D Turbulent MGD with the Generalized Ohm's Law," AIAA Paper 2001-2736, 2001.

[15] Gaitonde, D., and Poggie, J., "Elements of a Numerical Procedure for 3-D MGD Flow Control Analysis," AIAA Paper 2002-0198, 2002.

[16] McMullan, R., Lindsey, M., and Adamovich, I., "Experimental Validation of a 3-D Magnetogasdynamic Compressible Navier-Stokes Solver," AIAA Paper 2004-2269, 2004.

[17] Mitchner, M., and Kruger, C., *Partially Ionized Gases*, John Wiley and Sons, New York, 1973.

[18] Gaitonde, D., and Poggie, J., "Simulation of Magnetogasdynamic Flow Control Techniques," AIAA Paper 2000-2326, 2000.

[19] White, F., *Fluid Mechanics*, 2nd ed., McGraw–Hill, New York, 1986, Chap. 3.

[20] Heiser, W., and Pratt, D., *Hypersonic Airbreathing Propulsion*, AIAA Education Series, AIAA, Washington, DC, 1994.

[21] Litchford, R., Cole, J., Bityurin, V., and Lineberry, J., "Thermodynamic Cycle Analysis of Magnetohydrodynamic-Bypass Hypersonic Airbreathing Engines," NASA, Tech. Rept. TP-2000-210387, 2000.

[22] Kuranov, A., and Sheikin, E., "The Potential of MHD Control for Improving Scramjet Performance," AIAA Paper 1999-3535, 1999.

[23] Sagalyn, R., and Burke, H., *Air Force Handbook of Geophysics and the Space Environment*, National Technical Information Service, Springfield, VA, 1985, pp. 20-1–20-3.

[24] Nishihara, M., Jang, N., Rich, J., Lempert, W., and Adamovich, I., "Low-Temperature Supersonic Boundary Layer Control Using Repetitively Pulsed Magnetohydrodynamic Forcing," *Physics of Fluids*, Vol. 17, No. 10, 2005, pp. 106102-1–12.

[25] Kuranov, A., and Sheikin, E., "Magnetohydrodynamic Control on Hypersonic Aircraft Under 'Ajax' Concept," *Journal of Spacecraft and Rockets*, Vol. 40, No. 2, 2003, pp. 174–182.

[26] Kuranov, A., and Sheikin, E., "MHD Control on Hypersonic Aircraft under 'AJAX' Concept. Possibilities of MHD Generator," AIAA Paper 2002-0490, 2002.

[27] Macheret, S., Shneider, M., and Miles, R., "Potential Performance of Supersonic MHD Power Generators," AIAA Paper 2001-0795, 2001.

[28] Berger, M. J., "Stopping Powers for Electrons and Positrons," International Commission on Radiation Units and Measurements, Tech. Rept. ICRU-37, Bethesda, MD, 1984.

[29] Brichkin, D., Kuranov, A., and Sheikin, E., "The Potentialities of MHD Control for Improving Scramjet Performance," AIAA Paper 1999-4969, 1999.

[30] Holland, S. A., "Computational and Experimental Investigation of a Three-Dimensional Hypersonic Scramjet Inlet Flow Field," Ph.D. Dissertation, North Carolina State Univ., Raleigh, NC, 1991.

M. Auweter-Kurtz
Associate Editor